INTERNATIONAL JOURNAL FOR NUMERICAL METHODS IN FLUIDS
*Int. J. Numer. Meth. Fluids* **31**: 579–600 (1999)

# PREDICTION OF TURBULENT GAS–SOLIDS FLOW IN CURVED DUCTS USING THE EULERIAN–LAGRANGIAN METHOD

S. NAIK* AND I.G. BRYDEN

*Fluids and Environment Research Group, School of Mechanical and Offshore Engineering,*
*The Robert Gordon University, Schoolhill, Aberdeen AB9 1FR, UK*

## SUMMARY

The flow of particulate two-phase flow mixtures occur in several components of solid fuel combustion systems, such as the pressurised fluidised bed combustors (PFBC) and suspension-fired coal boilers. A detailed understanding of the mixture characteristics in the conveying component can aid in refining and optimising its design. In this study, the flow of an isothermal, dilute two-phase particulate mixture has been examined in a high curvature duct, which can be representative of that transporting the gas–solid mixture from the hot clean-up section to the gas turbine combustor in a PFBC plant. The numerical study has been approached by utilising the Eulerian–Lagrangian methodology for describing the characteristics of the fluid and particulate phases. By assuming that the mixture is dilute and the particles are spherical, the governing particle momentum equations have been solved with appropriately prescribed boundary conditions. Turbulence effects on the particle dispersion were represented by a statistical model that accounts for both the turbulent eddy lifetime and the particle transit time scales. For the turbulent flow condition examined it was observed that mixtures with small particle diameters had low interphase slip velocities and low impaction probability with the pipe walls. Increasing the particle diameters ($>50$ μm) resulted in higher interphase slip velocities and, as expected, their impaction probability with the pipe walls was significantly increased. The particle dispersion is significant for the smaller sizes, whereas the larger particles are relatively insensitive to the gas turbulence. The main particle impaction region, and locations most prone to erosion damage, is estimated to be within an outer duct length of two to six times the duct diameter, when the duct radius of curvature to the duct diameter ratio is equal to unity. Copyright © 1999 John Wiley & Sons, Ltd.

KEY WORDS: gas–solids flow; particles; Eulerian–Lagrangian; erosion; modelling; gas turbines

## 1. INTRODUCTION

There are a wide range of engineering components in the advanced generations of coal-fired plant, such as the pressurised fluidised bed combustors (PFBC), and in the standard pulverised coal suspension-fired systems, in which particulate flow occur. For example, in PFBC systems the hot gases laden with particulates from the coal combustor normally pass through a clean-up stage, where high temperature cyclones remove most of the particulates before the gas is directed to the gas turbine combustor. The ingress of particles into the gas turbine working environment is normally to be avoided in order to minimise the deterioration of the turbine

---

* Correspondence to: Base Technology, KWTB Turbomachinery Business Unit, ABB Power Generation Ltd., CH-5401, Baden, Switzerland.

CCC 0271–2091/99/190579–22$17.50

*Received January 1998*
*Revised April 1998*

blades both structurally and aerodynamically. As a significant amount of solid material needs to be pneumatically transported into and out of the major components of these plants, erosion can be a significant problem in the conveying ducts and in the components themselves. Such conveying ducts also exist between the mills and the burners of conventional pulverised coal-fired boilers. Here, they usually comprise of several curved sections, bends, vertical-to-horizontal transition sections and flow splitters (riffle boxes), which are also prone to erosion damage. To minimise erosion damage in such components, a detailed knowledge of the particulate flow behaviour can aid in refining and optimising their design.

Both laminar and turbulent single-phase flows in curved pipelines of square cross-sections have previously been examined in detail by Humphrey *et al.* [1,2] using hot-wire anemometry. Using the same flow configuration as Humphrey *et al.* [2], Platfoot and Fletcher [3] have computed both laminar and turbulent flows in the curved ducts using a 'non-elliptic' flow solver. A reasonable agreement between the predicted and experimentally obtained local velocities was reported. For flows consisting of a gas–solids mixture, Tsuji *et al.* [4], Lee and Durst [5] and Maeda *et al.* [6] determined experimentally the local velocities and turbulence intensities in a vertical straight circular duct for several conditions of particle sizes and concentrations. They reported that high concentrations and large particle sizes tends to dampen turbulence and can significantly alter the velocity profiles in the duct. Tsuji and Morikawa [7] have also conducted similar experimental studies for gas–solids flow in a horizontal circular pipe. For other configurations, such as pipe bends and tube bundles, the characteristics of the particulate two-phase flow and their erosion potential have been reported by Pourahmadi and Humphrey [8], Mason and Smith [9], Humphrey [10], Schuh *et al.* [11] and Beacher *et al.* [12]. More recently Tu and Fletcher [13] have computed gas–solids flow in a square sectioned 90° bend and compared their predictions with the laser Doppler anemometry (LDV) experimental data of Kliafas and Holt [14]. The computational method employed by Tu and Flectcher [13] was a Eulerian–Eulerian scheme for both the fluid and particulate phases, and good agreement of the local gas and particle velocities was reported for the limited experimental data available.

In the present numerical study, the flow of a dilute gas–solid mixture was initially examined in a vertical pipe and subsequently in a strongly curved, large aspect ratio rectangular duct. The Eulerian–Lagrangian methodology was employed and several assumptions were embodied in the algorithm regarding the particle motions. The effect of fluid turbulence on the particulate phase was represented by a statistical model, which accounts for both the turbulent eddy lifetime and the particle transit time scales.

## 2. MATHEMATICAL MODELLING

In order to obtain a detailed history of the particle velocities and trajectories within a flow field, it is necessary to know the detailed fluid flow field within the given geometry and how the two phases interact with each other. Within the Eulerian–Lagrangian methodology, the interaction between the phases is represented by the incorporation of the particle momentum influx–efflux terms into the governing conservation equations of the gas phase, Migdal and Agosta [15]. This methodology is generally referred to as the particle source-in-cell method (PSI-Cell), Crowe *et al.* [16].

This momentum coupling between the phases for gas–solid mixtures is relevant when the particulate suspension is significant and if it modifies the fluid flow characteristics due to its presence in the flow. For dilute suspensions, which are characterised by mass loading ratios of $< 1$, it is appropriate to assume that the influence of the particulate phase on the carrier fluid is minimal. The experimental data of Tsuji *et al.* [4] and Lee and Durst [5] confirm this assumption. Tsuji *et al.* [4] and Lee and Durst [5] have, however, also shown that in mixtures with high mass loadings ($> 1$) and large particle diameters ($> 200$ μm), the fluid flow field can be significantly perturbed by the presence of the particles. More recently, Pan and Banerjee [17] indicate from a direct numerical simulation (DNS) of 'large' particles in an open channel, low Reynolds number flow, that even at low concentration ($\approx 10^{-4}$), the presence of these 'large' particles enhances turbulence production. This was particularly observed in the near-wall region, where a large enhancement in the Reynolds stresses was predicted. For 'small' particles, which are smaller than the smallest turbulent length scales, Elghobashi and Truesdell [18] have also shown via a DNS method, that their presence in a low Reynolds number decaying homogenous turbulent field, can increase the turbulent dissipation. In both the latter studies, the 'two-way coupling' between the phases was assumed.

In the present study, high Reynolds number ($> 10^4$) flows are studied and the considered mixtures have mass loading ratios $< 1.0$, with 80% of the particulate concentration consisting of particles $< 200$ μm. The coupling of the phases through their momentum interactions has not been modelled and only 'one-way coupling' has been assumed.

### 2.1. Fluid phase

The fluid phase characteristics are represented by the steady state, time-averaged, incompressible, conservation equations of mass and momentum. For flows in non-orthogonal curvilinear co-ordinates, these conservation equations can be represented in tensor notation in terms of the Cartesian velocity, $u$, by (Peric *et al.* [19], Rodi *et al.* [20], Majumdar *et al.* [21]);

*Mass conservation*

$$\frac{1}{J}\frac{\partial}{\partial \xi_j}(\rho u_m \beta^j_m) = 0. \tag{1}$$

*Momentum conservation*

$$\frac{1}{J}\frac{\partial}{\partial \xi_j}((\rho u_m u_i - D_{mi})\beta^j_m) = 0, \tag{2}$$

where

$$D_{mi} = -P\delta_{mi} + \frac{1}{J}\mu_{\text{eff}}\left(\frac{\partial u_i}{\partial \xi_n}\beta^n_m + \frac{\partial u_m}{\partial \xi_l}\beta^l_i\right),$$

and $\beta$ represents the cofactors of $\partial x_i/\partial \xi_j$ in the Jacobian of the co-ordinate transformation $x_i = x_i(\xi_j)$, which are defined by

$$\beta^1_1 = \frac{\partial y}{\partial \eta} = y_\eta, \tag{3}$$

$$\beta^2_1 = -\frac{\partial y}{\partial \xi} = -y_\xi, \tag{4}$$

$$\beta^1_2 = -\frac{\partial x}{\partial \eta} = -x_\eta, \tag{5}$$

$$\beta^2_2 = \frac{\partial x}{\partial \xi} = x_\xi. \tag{6}$$

Figure 1 shows the above geometrical relationships for one of the computational cell faces (i.e. the east cell face, e), which can be easily determined from the co-ordinates of the quadrilateral non-orthogonal cell vertices.

The above conservation equations (1) and (2) are solved in conjunction with the two-equation $k$–$\varepsilon$ model of turbulence (Jones and Launder [22]), which assumes that the gas turbulence is locally isotropic. The kinetic energy of turbulence, $k$, and its dissipation, $\varepsilon$, in the $k$–$\varepsilon$ model are described by

*Turbulence energy*, *k*

$$\frac{1}{J}\frac{\partial}{\partial \xi_j}((\rho u_m k - F_m)\beta_m^j) = G - \rho\varepsilon, \tag{7}$$

where

$$F_m = \frac{1}{J}\frac{\mu_{\text{eff}}}{\sigma_k}\frac{\partial k}{\partial \xi_n}\beta_m^n$$

and the rate of production of turbulent energy, $G$, is defined by

$$G = \frac{\mu_{\text{eff}}}{J}\left(\frac{\partial u_i}{\partial \xi_n}\beta_j^n + \frac{\partial u_j}{\partial \xi_n}\beta_i^m\right)\frac{\partial u_i}{\partial \xi_n}\beta_j^n.$$

*Dissipation of turbulence energy*, *ε*

$$\frac{1}{J}\frac{\partial}{\partial \xi_j}((\rho u_m \varepsilon - F_m)\beta_m^j) = C_1\frac{\varepsilon}{k}G - C_2\rho\frac{\varepsilon^2}{k}, \tag{8}$$

where

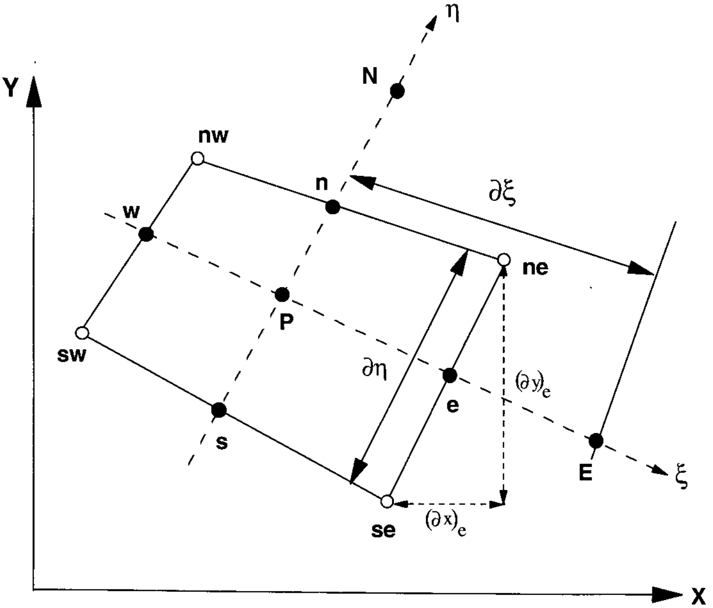

Figure 1. Geometrical representations of a non-orthogonal computational cell.

Table I. Empirical constant used in the $k$–$\varepsilon$ turbulence model (Launder and Spalding [23])

| Constant | $C_\mu$ | $C_1$ | $C_2$ | $\sigma_k$ | $\sigma_\varepsilon$ |
|---|---|---|---|---|---|
| Value | 0.09 | 1.44 | 1.92 | 1.0 | 1.3 |

$$F_m = \frac{1}{J}\frac{\mu_{\text{eff}}}{\sigma_\varepsilon}\frac{\partial \varepsilon}{\partial \xi_n}\beta^n_m.$$

The effective viscosity $\mu_{\text{eff}}$ in Equations (2), (7) and (8) is determined from (Jones and Launder [22])

$$\mu_{\text{eff}} = \mu + \mu_{\text{T}}, \tag{9}$$

where the turbulent viscosity is defined by

$$\mu_{\text{T}} = C_\mu \rho \frac{k^2}{\varepsilon}. \tag{10}$$

The empirical constants that are contained within Equations (7), (8) and (10) are given by Table I, as recommended by Launder and Spalding [23].

In order to solve the above conservation equations, they are discretised using the finite volume method. This results in a quasi-linear equation for each control volume cell, which is of the form

$$a_{\text{p}}u_{i\text{p}} + \sum_m a_m u_{i,m} = S_u, \tag{11}$$

where the subscript $m$ represents the eight neighbouring nodes of node $P$ (i.e. e, w, n, s, ne, nw, se, sw as shown in Figure 1). The coefficient $a$ contains contributions from both the convection and diffusion fluxes, the exact formulations of which are described by Peric *et al.* [19], and $S_u$ contains the pressure force component in the direction of the velocity component $u_i$. The velocities $u_{i,m}$ are the values of the velocity component $u_i$ at the computational points residing in the neighbouring control volumes.

In Equation (11) the convection terms contained in the coefficient $a$ are discretised using the linear upwind differencing scheme, Patankar [24], which is second-order-accurate. And, the diffusion terms in the coefficient $a$ are expressed by the central difference approximations, which is also second-order-accurate, Patankar [24] and Gosman *et al.* [25]. The cross-derivative terms that result in the diffusion components due to the non-orthogonal grids are discretised using linear interpolation.

The pressure field, which is represented by the source terms in Equation (11), is solved using the momentum interpolation method of Rhie and Chow [26], in conjunction with the SIMPLE pressure-correction algorithm of Patankar and Spalding [27]. The use of this practice and the equations obtained are based on those outlined by Peric [19,28] and Mumjumar *et al.* [21].

Finally, the solution of Equation (11), which consists of a large number of non-linear equations and which requires an iterative procedure, is obtained by using the strongly implicit procedure of Stone [29]. In this iterative solution procedure, underrelaxation is employed to allow for stable convergence of the equations. Convergence for the set of equations that result from Equation (11) is determined by monitoring the change in the normalised sum of the residuals between iterations, Patankar [24], and also by monitoring the change in the values of every variable (e.g. velocities, pressure, $k$ and $\varepsilon$) at prescribed locations within the computational domain. These prescribed locations are strategically located within the computational domain and generally correspond to areas where the variables to be solved are likely to vary the most, e.g. within a flow recirculation zone. For the cases examined in the present study, it was found that by employing underrelaxation factors of 0.2 for pressure and 0.75 for the velocities and $k$ and $\varepsilon$, convergence can be achieved within 500 iterations, when the convergence criteria for the normalised sum of the residuals is prescribed to be $10^{-4}$.

### *2.2. Particulate phase*

The dilute gas–solids two-phase mixture considered in this study is characterised by a volume fraction of $<10^{-3}$, a mass loading ratio $<1$ and a density ratio $\rho_p/\rho \cong 10^3$. Under these assumptions it is sufficiently accurate to assume that the particles are non-interacting (Humphrey [10] and Clift *et al.* [30]). That is, the dynamics of any one particle are not influenced by the presence of neighbouring particles (either directly, through collisions, or indirectly, through the perturbed fluid field). Ash particles from the hot gas clean-up section of a PFBC plant or pulverised coal particles being transported to the coal burners in a coal fired boiler would normally satisfy the density ratio conditions, where $\rho_p/\rho$ is typically of the order of $10^3$. The volume fractions and mass loading ratios in such systems also tend to be of the order of $10^{-4}$ and 0.3 respectively (Lawn [31]), which ensures that all the conditions for non-interacting particles are satisfied.

The instantaneous velocity of a single spherical particle of diameter $d_p$ can then be determined from the conservation equation of particle momentum, i.e.

$$m_p \frac{dV_{pi}}{dt} = \frac{1}{2} C_D \rho A_p (V_{fi} - V_{pi}) |\bar{V}_f - \bar{V}_p| + m_p g_i, \tag{12}$$

assuming that the particles are spherical, non-interacting and that there are negligible additional forces except for those due to drag and gravity. Due to the high ratio of the particle to gas densities, other forces, such as the apparent mass, pressure gradient, Basset and the two lift forces due to fluid shearing and particle rotation, are small.

The particle drag coefficient, $C_D$, for rigid spherical particles in Equation (12) is determined from Clift *et al.* [30], where

$$C_D = \frac{24}{Re}(1 + 0.15 Re^{0.687}) \quad \text{for} \quad 0 < Re < 10^3 \tag{13}$$

and the Reynolds number is defined as

$$Re = \rho d_p |\bar{V}_f - \bar{V}_p| / \mu, \tag{14}$$

where

$$|\bar{V}_f - \bar{V}_p| = \sqrt{(U_f - U_p)^2 + (V_f - V_p)^2}\,.$$

The position of the particle within the computational domain can be described by its rate of change with respect to time, i.e.

$$\frac{dx_{pi}}{dt} = V_{pi}. \tag{15}$$

The above Equations (12)–(15) describe the instantaneous velocities and positions of the particle within the flow field and the solution of these equations can be obtained by using a number of numerical methods (e.g. Runge–Kutta, Euler, etc.). In the present study they have been solved by direct integration. The required time steps in Equations (12) and (15) are determined from the shorter of the two times required by the particle to traverse the width or length of the cell at its current velocity in the respective directions, i.e.

$$t = \min\left(\frac{\Delta x}{U_{\mathrm{p}}}, \frac{\Delta y}{V_{\mathrm{p}}}\right)\alpha,$$

where $\alpha$ is a prescribed factor. Depending on the cell aspect ratio, this prescribed factor determines the 'coarseness' of the time step. The effect of several values of the prescribed factors on the predicted particle velocities and trajectories were examined in order to ascertain time step independent solutions. For the two cases examined in this study, a factor of $\frac{1}{3}$ for cell aspect ratios $< 2$ indicated that the predicted velocities and trajectories were reasonably time step independent.

### 2.3. Turbulent dispersion of the particulate phase

In order to account for the influence of gas turbulence on the particle dispersion, the 'time scale' model of Dukowicz [32], Gosman and Ioannides [33] was employed. In this approach, the instantaneous fluid velocity in Equation (12) is decomposed into its mean and fluctuating component via

$$V_{\mathrm{f}i} = \bar{V}_{\mathrm{f}i} + \sigma_i\sqrt{(2k/3)}, \tag{16}$$

where the second term on the right-hand-side of Equation (16) is the fluctuating gas velocity, which is assumed to have a Gaussian probability distribution, and $\sigma_i$ is a normally distributed random number with a zero mean and unit variance. As the particle traverses a turbulent eddy, the interaction time of this randomly sampled gas fluctuating velocity component, with the particle is limited by the lifetime of the turbulent eddy, $t_{\mathrm{e}}$, or the transit time for the particle to traverse the eddy, $t_{\mathrm{r}}$, i.e.

$$t_{\mathrm{int}} = \min\,(t_{\mathrm{e}}, t_{\mathrm{r}}), \tag{17}$$

where $t_{\mathrm{e}} = l_{\mathrm{e}}/|v_{\mathrm{f}i}|$ and the eddy length scale $l_{\mathrm{e}} = C\mu^{3/4}k^{3/2}/\varepsilon$. The transit time $t_{\mathrm{r}}$ can be determined from the linearised form of the particle momentum equation, Gosman and Ioannides [33], i.e.

$$t_{\mathrm{r}} = -\tau\ \ln\left(1 - \frac{l_{\mathrm{e}}}{(\tau|\bar{V}_{\mathrm{f}} - \bar{V}_{\mathrm{p}}|)}\right), \tag{18}$$

where the particle relaxation time is $\tau = \rho_{\mathrm{p}}d_{\mathrm{p}}^2/18\mu f$, with $f = C_{\mathrm{D}}Re/24$. After each interaction between the particle and the turbulent eddies, a new fluctuation is assumed as the particle traverses the flow field.

### 2.4. Boundary conditions

For the gas phase, the velocities and turbulence properties are specified at the inlet domain and a zero gradient condition is specified at the outlet to represent fully developed conditions. At the solid walls, computations of the boundary layer and its representation is evaluated from the 'log-law' wall relationships, using the wall functions approach of Launder and Spalding [23].

For the particulate phase, the inlet velocities are statistically prescribed, with the instantaneous inlet velocity being composed of a mean and a randomly sampled fluctuating component. When the particles approach the wall boundary, the 'stopping distance' model of

Friedlander and Johnstone [34] has been adopted. Particles approaching a wall penetrate its boundary layer and subsequently strike the wall only if they possess a ‘stopping distance’, stretching from the edge of the boundary layer to the wall, which is greater than the boundary layer thickness. In this study it is assumed that the laminar sublayer extends to a normal dimensionless distance $y^+ = 11.63$ from the wall, and the normal particle velocity at this distance is its instantaneous normal value. As all the computational cells are quadrilateral elements, the normal distance from the wall is evaluated from a knowledge of the co-ordinates of the wall cell vertices. The stopping distance is then evaluated from the particle instantaneous normal velocity at $y^+ = 11.63$ and its relaxation time assuming that the laminar sublayer is stagnant. Those particles attaining $y^+ < 11.63$ are trapped and move with the sublayer, while particles with $y^+ > 11.63$ penetrate the sublayer and strike the wall surface. The striking particles then rebound from the wall subject to a normal and tangential coefficient of restitution. Referring to Figure 2, the rebound velocities are calculated by first determining the normal and tangential particle velocities from

$$V_t = U_p \cos\theta + V_p \sin\theta, \tag{19}$$

$$V_n = -U_p \sin\theta + V_p \cos\theta. \tag{20}$$

The rebound velocity components normal and tangential to the wall are then calculated using appropriate restitution coefficients, according to

$$V'_n = -e_n V_n, \tag{21}$$

$$V'_t = e_t V_t. \tag{22}$$

Finally, the rebound velocity in the original co-ordinate system is computed from

$$U'_p = V'_t \cos\theta - V'_n \sin\theta, \tag{23}$$

$$V'_p = V'_t \sin\theta + V'_n \cos\theta. \tag{24}$$

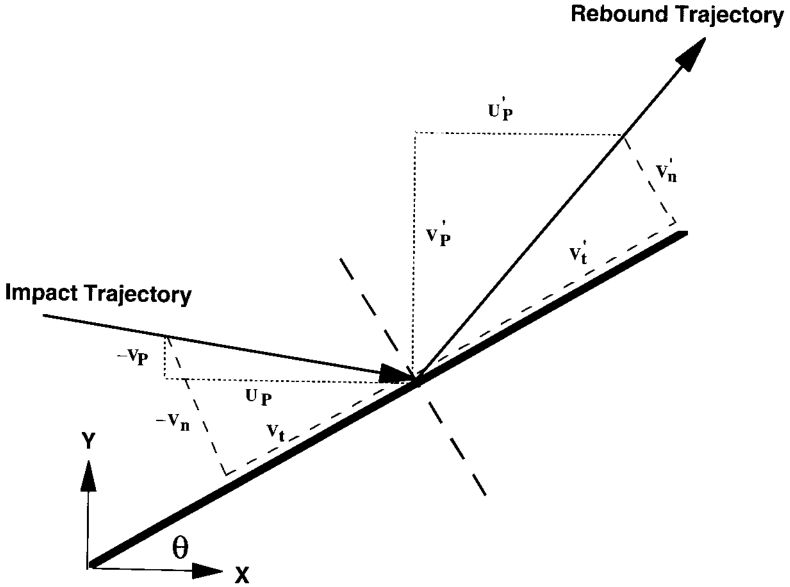

Figure 2. Particle boundary conditions at a solid wall.

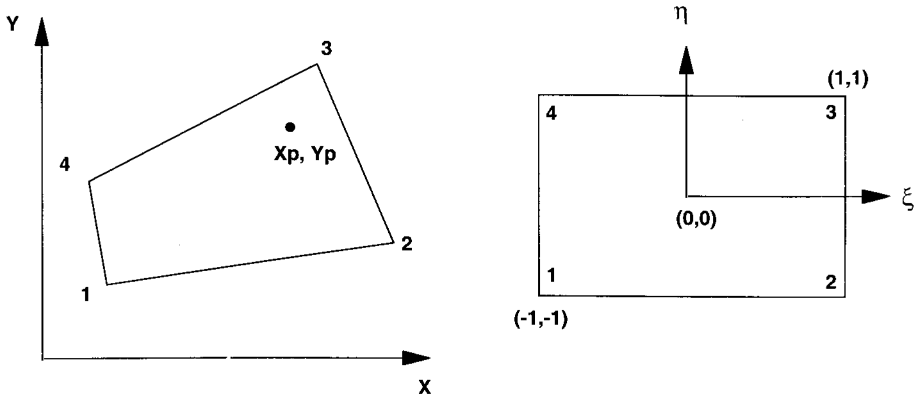

Figure 3. Transformation of a computational cell from global to local co-ordinates.

In the absence of sufficient experimental data on the distribution of the restitution coefficients with respect to the particle impaction and rebound angles to the wall and the particle/wall material combinations, the data of Brauer [35] have been utilised. For the present study, it has been assumed that the normal and tangential restitution coefficients are 0.9 and 0.8 respectively.

## 2.5. Particle tracking

As the computational grid employed in the present study is non-orthogonal, accurate tracking of the particles within the computational domain is required. In this study particle tracking is initiated by initially 'sweeping' the computational domain and the particle positions compared with the minimum and maximum positions of the cell vertices of the 'swept' cell. If the particle co-ordinates fall within this range, then it may reside in that cell or any one of its eight surrounding neighbouring cells. In order to precisely determine the cell location, the global co-ordinates of the cell are temporarily transformed into a local co-ordinate system, as shown by Figure 3, by expressing the global co-ordinates of the transformed cell in terms of their nodal values via

$$x_{\mathrm{p}}^{\circ} = \sum_{k=1}^{4} \phi_k(\xi, \eta) x_k, \tag{25}$$

$$y_{\mathrm{p}}^{\circ} = \sum_{k=1}^{4} \phi_k(\xi, \eta) y_k, \tag{26}$$

where $\phi_k$ is the quadrilateral cell shape function defined by (Akin [36])

$$\phi_k(\xi, \eta) = \frac{1}{4}(1 + \xi_{\mathrm{p}}^{\circ}\xi_k)(1 + \eta_{\mathrm{p}}^{\circ}\eta_k), \tag{27}$$

with $k = 1-4$ representing the four nodal values of the cell. The Jacobian relating the global and local co-ordinates is then determined from

$$J = \left[\frac{\partial \phi_k}{(\partial \xi_{\mathrm{p}}^{\circ})_j}\right][x_{kj}] \tag{28}$$

and the inverse of this Jacobian will contain the derivatives

$$\frac{\partial \xi}{\partial x}, \quad \frac{\partial \xi}{\partial y}, \quad \frac{\partial \eta}{\partial x}, \quad \frac{\partial \eta}{\partial y}.$$

The particle position in the local co-ordinates can then be computed from

$$\xi_{\mathrm{p}} = \xi_{\mathrm{p}}^{\circ} + \frac{\partial \xi}{\partial x}(x_{\mathrm{p}} - x_{\mathrm{p}}^{\circ}) + \frac{\partial \xi}{\partial y}(y_{\mathrm{p}} - y_{\mathrm{p}}^{\circ}), \tag{29}$$

$$\eta_{\mathrm{p}} = \eta_{\mathrm{p}}^{\circ} + \frac{\partial \eta}{\partial x}(x_{\mathrm{p}} - x_{\mathrm{p}}^{\circ}) + \frac{\partial \eta}{\partial y}(y_{\mathrm{p}} - y_{\mathrm{p}}^{\circ}). \tag{30}$$

Assuming an initial value of $\xi_{\mathrm{p}}^{\circ}$ and $\eta_{\mathrm{p}}^{\circ}$, which should lie within the quadrilateral cell (e.g. 0, 0), Equations (29) and (30) can be solved iteratively. This will then produce an accurate transformation of the particle global co-ordinates $x_{\mathrm{p}}$, $y_{\mathrm{p}}$, into the local co-ordinate system. If the local co-ordinates from Equations (29) and (30) lie within the transformed rectangular cell, then the cell of the computational domain containing the particle is located, otherwise solution is shifted to the next neighbouring cell. It has been found in practice, that less than ten iterations are required to achieve convergence and the whole computational domain can be 'sweeped' very quickly.

## 3. RESULTS AND DISCUSSIONS

### 3.1. *Gas–solids flow in a vertical pipe*

Initially, the vertically upward flow of a dilute gas–solid mixture was simulated in a vertical pipe and compared with the LDV experimental data of Tsuji *et al.* [4]. For these predictions, the axisymmetric form of the gas and particulate transport equations (1)–(3) were employed. The vertical pipe considered was of internal diameter 30.5 mm and subjected to a air Reynolds number of $3.8 \times 10^4$ and a mean air inlet velocity of 18.9 m s$^{-1}$. The particulate phase consisted of 200 μm diameter spherical particles with a density 1020 kg m$^{-3}$ and the mass loading for the mixture was 1.0. At the inlet the particles were assumed to be uniformly distributed with a inlet velocity of 16.2 m s$^{-1}$, which was obtained by taking the average of the particle velocity profile determined experimentally by Tsuji *et al.* [4].

Figure 4 shows the gas and particulate flow mean velocities and turbulent intensities at fully developed flow conditions 75 pipe diameters from the inlet. It is evident that there is generally a good agreement between the predicted and experimental data. Although at the wall the predicted air turbulence intensities are slightly underpredicted, they show the general trend of high values near the wall shear layer and lower values in the bulk of the flow.

For the particulate phase, the computed mean velocities also agree favourably with the experimental data, although they are slightly overpredicted across the whole pipe radius. As the particle size (200 μm) considered is large, there is a large interphase slip velocity between the gas and particulate phases particularly in the central core of the pipe. Towards the wall the experimental results of Tsuji *et al.* indicate that the particles have higher velocities than the gas. Lee and Durst [5] also observed this in their studies and indicated that this was due to the shear induced lift force acting on the particle, which they did not find when the particle diameters are less than 200 μm. Figure 4 also shows a comparison between the predicted and experimental gas turbulence intensities. In this figure only the predicted particle turbulent intensities are shown due to lack of experimental data. It is evident from Figure 4 that the particle turbulence intensities lag the gas phase by a factor greater than 5. Although large particles are relatively insensitive to the fluid turbulence, Tsuji *et al.* indicate that at high mass loading ( > 1.0), the effect of increasing particle sizes from 200 μm to 3 mm increases the fluid turbulence, and that a much flatter gas velocity distribution ensues across the pipe diameter.

### *3.2. Gas–solid flow in a high curvature duct*

In order to examine the isothermal flow of a dilute gas–solid mixture in a high curvature duct, a horizontal to vertical large aspect ratio rectangular duct, which is connected by a tight 90° bend, was utilised. The geometry of the duct is indicated by Figure 5. By considering a duct with an aspect ratio $\gg 1$, it has been assumed that the influence of secondary flows on the mean gas and particulate flow characteristics is small. Pourahmadi and Humprey [8], who examined gas–solids flow in a duct with a radius of curvature to duct diameter ratio of 12, indicate that this is a reasonable assumption for the prediction of engineering flows. Recently, Tu and Fletcher [13], who have used the experimental data of Kliafas and Holt [14] in their numerical study, have also shown that for a duct with a radius of curvature to duct diameter ratio of 1.76, the influence of the velocity displacement that results from the secondary flows in curved ducts has a negligible effect on the particle mean velocities when they are 50 μm or 100 μm in size.

In the present study, the gas flow field in the duct, of width 0.27 m, was computed at a Reynolds of $2 \times 10^5$ with a mean inlet gas velocity of 15 m s$^{-1}$. The radius of curvature of the duct bend was 0.27 m. At the inlet a non-uniform gas velocity and turbulence intensity profile was prescribed, with an assumed distribution equal to the predicted fully developed pipe flow conditions shown by Figure 4. The computations for the gas phase were initially performed with four non-uniform grid distributions, namely $12 \times 60$, $20 \times 80$, $24 \times 102$ and $35 \times 160$. In all cases the cell aspect ratios were kept $< 2$ in the vicinity and within the curved section, and the streamwise grid lines were aligned parallel to anticipated fluid streamlines in order to minimise numerical diffussion, Patankar [24]. Additionally, a fine mesh was prescribed near the two duct walls and within the 90° bend. The convergence criteria (sum of the normalised residuals) for all the computed variables was maintained at $10^{-4}$. It was found that the

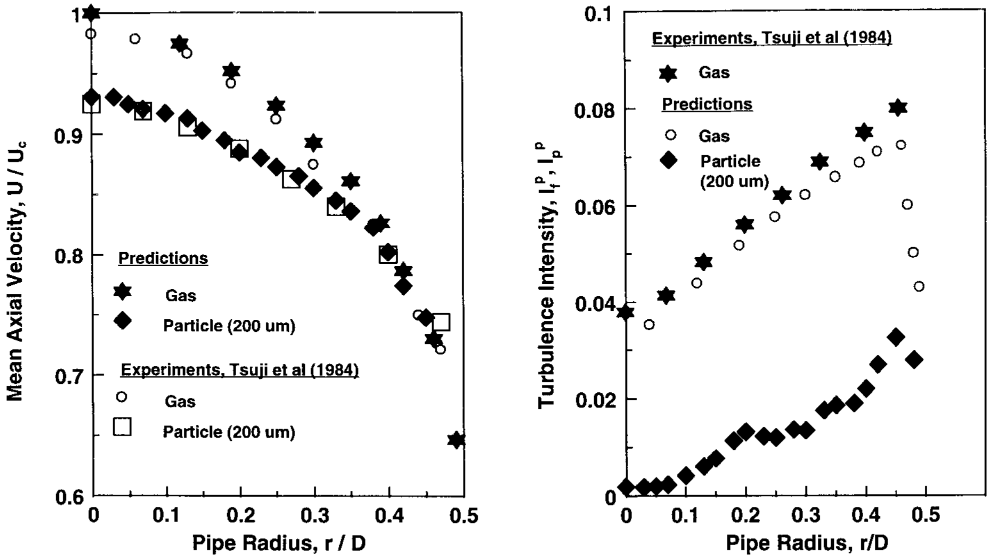

Figure 4. Gas and particle mean velocities and turbulence intensities in a vertical pipe.

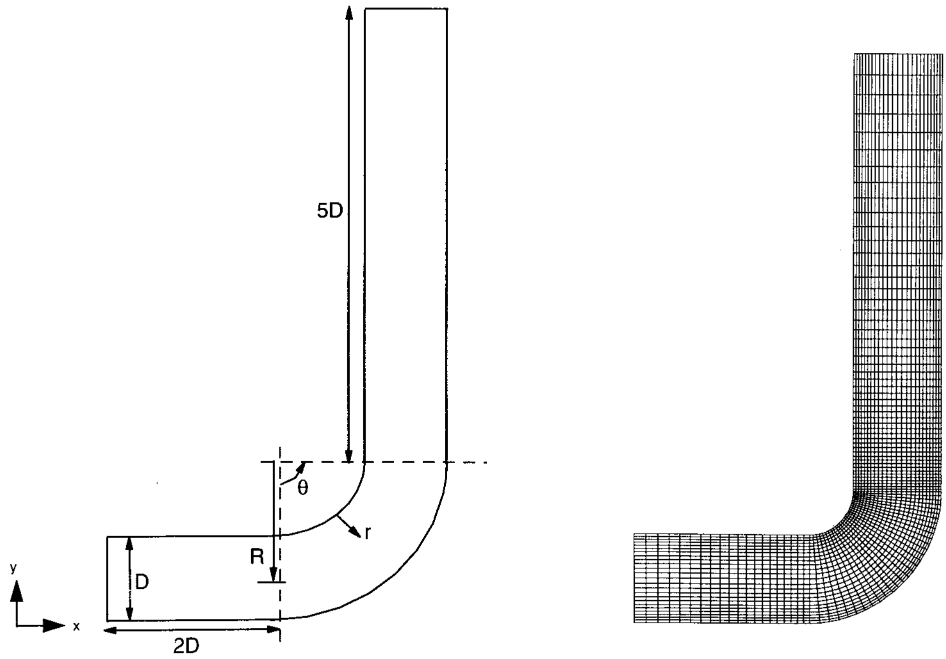

Figure 5. Geometry of the curved duct and the employed computational grid.

maximum difference in the streamwise and transverse velocity profiles between the 24 × 102 and the 35 × 160 grids was less than 1.2%, and hence in order to maintain computational efficiency, the 24 × 102 grid was subsequently used for all the simulations.

For the particulate phase, the mean inlet velocities were 12.9, 13.6, 14.2 and 14.8 m s$^{-1}$ for the 200, 100, 50 and 10 μm particle sizes respectively. The inlet velocity distribution for the 200 μm was assumed to have the same profile to that indicated by Figure 4 corresponding to fully developed conditions. Velocity distributions similar to that shown by Figure 4 were also computed for the 100, 50 and 10 μm particles (not shown) and their fully developed profiles were used as initial inlet conditions to the duct. The density of the particles was 1020 kg m$^{-3}$ and the mass loading was assumed to be 0.05. At each inlet starting location, the particulate stream consisted of the following particle sizes and fractions: 10 μm (25%), 50 μm (50%), 100 μm (20%) and 200 μm (5%). In order to maintain statistical significance, several tens of thousand particles of each size fraction were injected at each starting location of the inlet boundary.

### *3.3. Particle trajectories*

Figure 6 shows some of the several thousands of the computed trajectories of the 10, 50, 100 and 200 μm particle sizes. They are shown separately to keep the clarity of the illustration. As expected, the smaller particles (10 μm) tend to follow the fluid streamlines in most of the duct, with some of the particles being influenced by the centrifuging effect in the bend. As the particle size is increased to 50 μm, this centrifuging effect becomes more prominent, with only some of the particles flowing near the inner wall of the vertical section of the pipe. For both of these smaller particles sizes, Figure 6 illustrates that due to the influence of the fluid turbulence, all the particles injected from a point source at the inlet, begin to disperse transversely within the horizontal pipe section immediately after injection.

When the particle size is increased to 100 and 200 μm, their inertia markedly influences the particle trajectory paths. On entering the bend, very few of these particles respond to the fluid streamlines and their inertia carries them towards the outer wall of the duct. The majority of these large particles after striking the outer wall, become re-entrained into the bulk flow. For the 200 μm particles, the frequency of particle impacts with the bend outer wall is quite significant and after rebound, some of these particles are projected on a collision trajectory with the opposite inner wall much further downstream. These trajectories result mainly due to their higher inertia. Qualitatively similar observations have also been reported by Pourahmadi and Humphrey [8], Tu and Fletcher [13] and Kliafas and Holt [14]. The larger particles are also relatively insensitive to the turbulent eddies. As Figure 6 shows, the transverse particle dispersion after injection within the horizontal duct section, is significantly less compared to that predicted for the smaller particles.

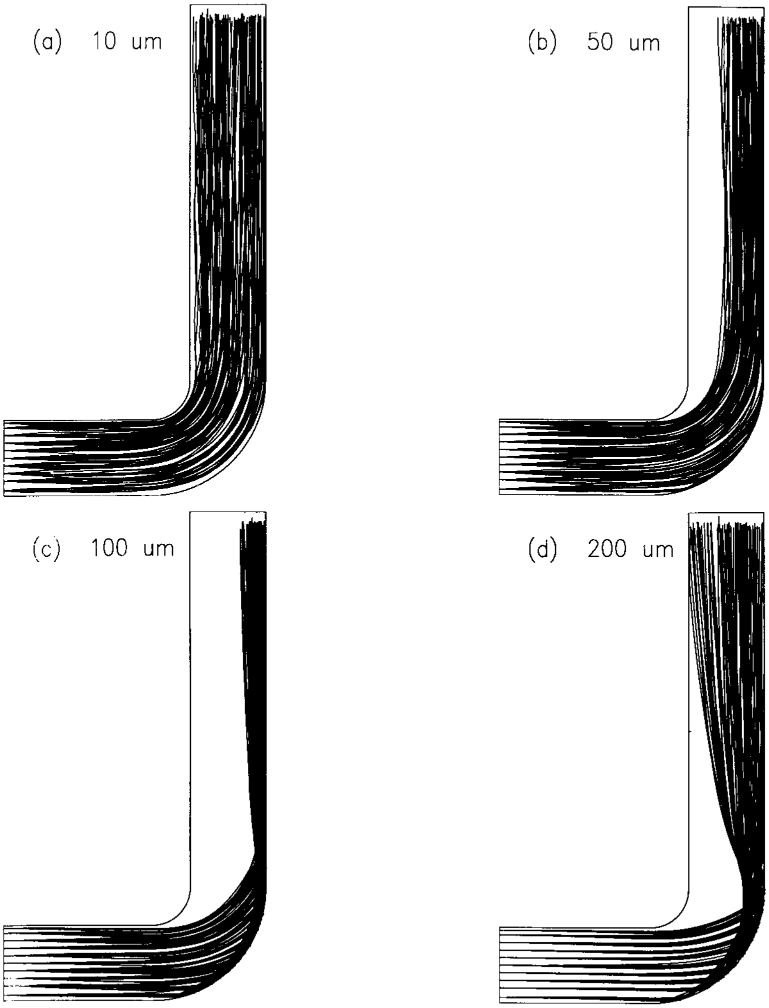

Figure 6. Particle trajectories in curved duct for (a) 10 μm, (b) 50 μm, (c) 100 μm, and (d) 200 μm particle sizes.

### *3.4. Velocity distributions*

The mean velocities of all the particle sizes are indicated by Figures 7 and 8 in conjunction with the mean absolute gas velocities. As the particles approach the curved section (at $\theta = 0°$), the smaller particles have low slip velocities, and in the bulk of the flow their mean velocities are similar to the absolute mean gas velocity. The larger particles, have lower horizontal velocities particularly near the inner wall of the curved duct whereas at the outer wall, their velocities are higher than that of the gas phase. The vertical velocity components at the inlet to the curved section for all the particles sizes (Figure 8) are very small as the flow is predominately horizontal.

As the flow progresses further into the curved section ($\theta = 30°$), the higher gas velocities at the inner duct wall are evident from Figure 7. The larger particles in this section have a higher horizontal velocity component than the carrier fluid particularly towards the outer wall section. Unlike the smaller particles, the motion of the larger particles is dominated by their inertia and hence they deviate considerably from the gas streamlines within the curved section. This can be observed from Figures 7 and 8, which show that they have a high horizontal velocity component but a relatively smaller magnitude of the vertical velocity.

At ($\theta = 60°$), the horizontal velocity of the smaller particles within the whole duct section decreases further with a corresponding increase in the vertical mean velocities as they follow the gas streamlines. The larger particles in contrast, however, deviate from the fluid streamlines considerably and hence still retain a higher horizontal mean velocity with an increasing vertical component. At this section of the channel, a clustering of the larger particles is evident near the outer wall which is largely due to the centrifuging effects. Additionally, for the 200 μm particles, Figures 7 and 8 show that the mean velocities are only present in the central bulk of the flow that correspond to the particle positions after they have rebounded from the outer wall. At the bend outlet ($\theta = 90°$), the mean horizontal velocities of all the particle sizes decrease, with the vertical velocity component dominating the mean motion of the particles.

### *3.5. Turbulence characteristics*

The turbulence intensities of the gas and particulate phases within the transverse and longitudinal planes of the duct geometry are illustrated in Figure 9. Both the gas and particulate phase intensities have been normalised with respect to the mean gas inlet velocity.

At the inlet to the bend ($\theta = 0°$), the gas phase has the characteristic turbulence intensity profile of pipe flow. High values are predicted near the walls where the greatest fluid shearing exist, with lower and almost constant values being attained in the bulk of the central core. Tu and Fletcher [13] show similar distributions in the gas-phase turbulence intensities, but indicate that the $k$–$\varepsilon$ model tends to overpredict the intensities, particularly downstream from the bend inlet and at the inner wall of the duct. For the particulate phase, Figure 9 shows that the smaller 10 μm particles have the same trend in the turbulence intensity profiles as the gas phase except they have lower magnitudes. The larger particles also show similar profiles to the gas phase although their magnitudes are also lower than the smallest particles considered. Tsuji *et al.* [4] and Durst *et al.* [5] have, however, shown that if the gas–solid mixture mass loading is high ($>1$), the influence of particle sizes of 200 μm and less tend to dampen the gas turbulence, whereas when they are greater than 200 μm, their presence increases the gas turbulence and creates a much flatter gas velocity profile. In the present study it has been assumed that the gas–solid mixture is very dilute and hence the influence of the particulate phase on the gas phase is small, which is collaborated by the experimental data of Tsuji *et al.* [4].

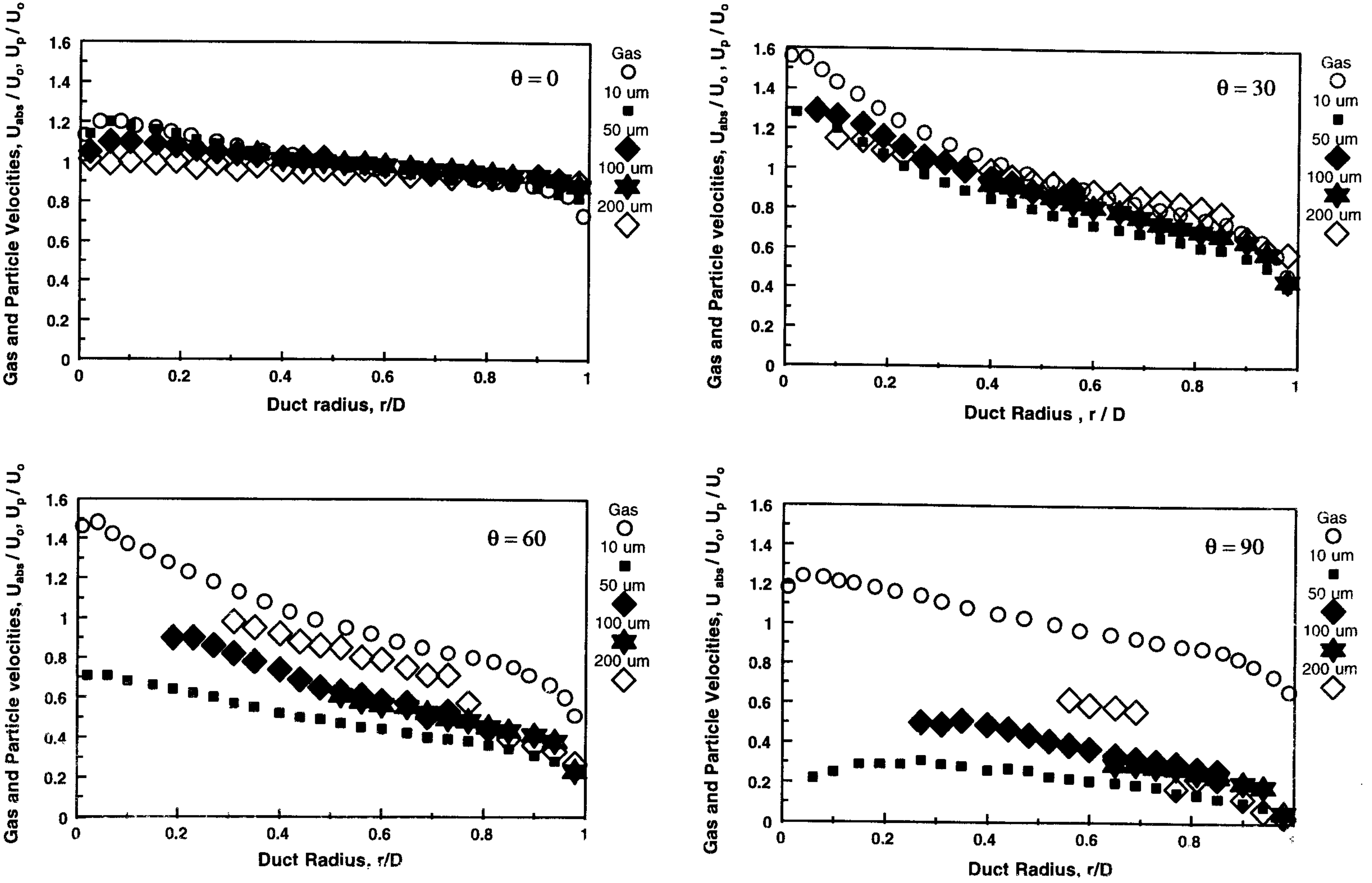

Figure 7. Absolute gas velocities and particle *horizontal* velocities in the curved duct.

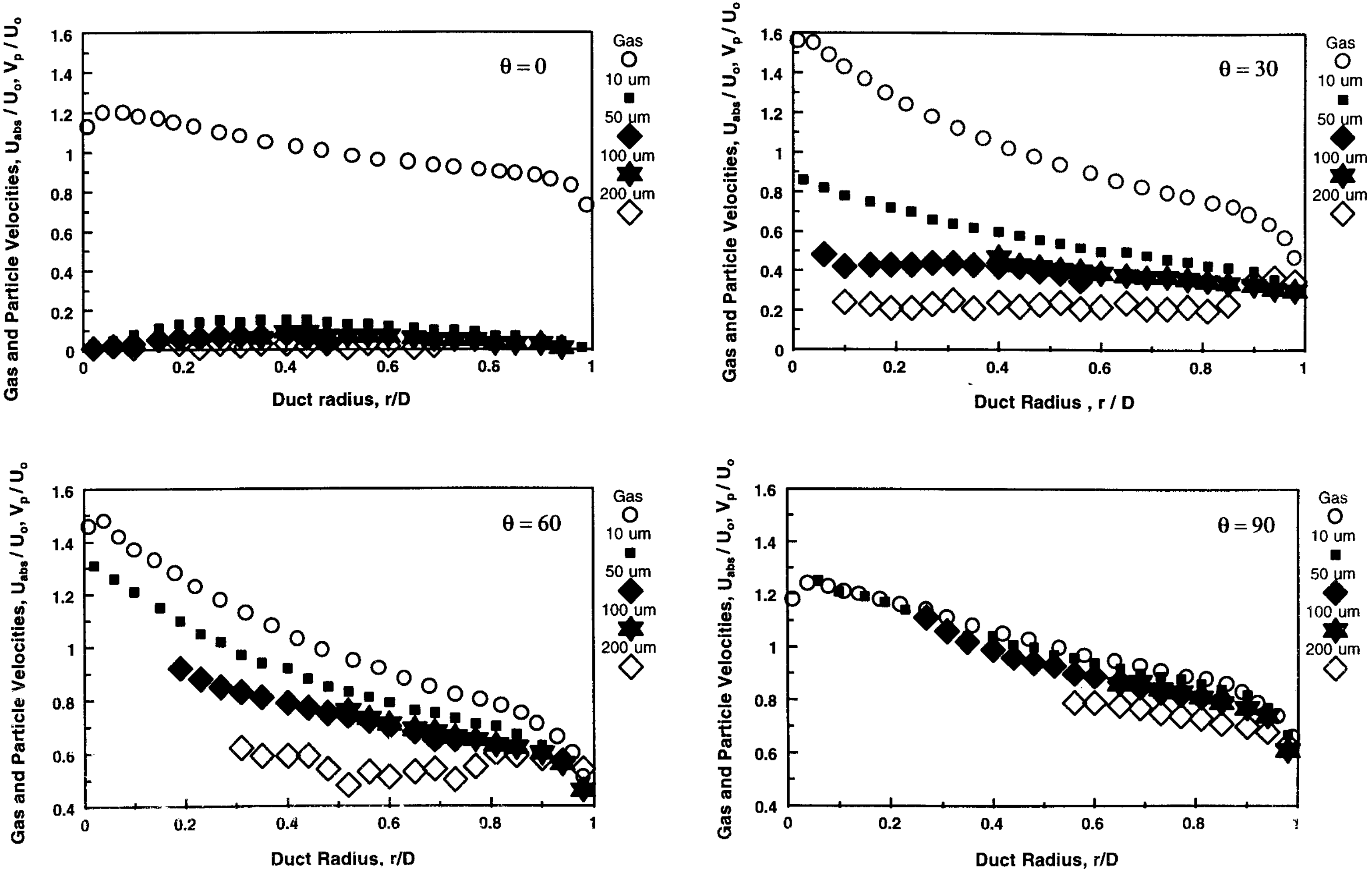

Figure 8. Absolute gas velocities and particle *vertical* velocities in the curved duct.

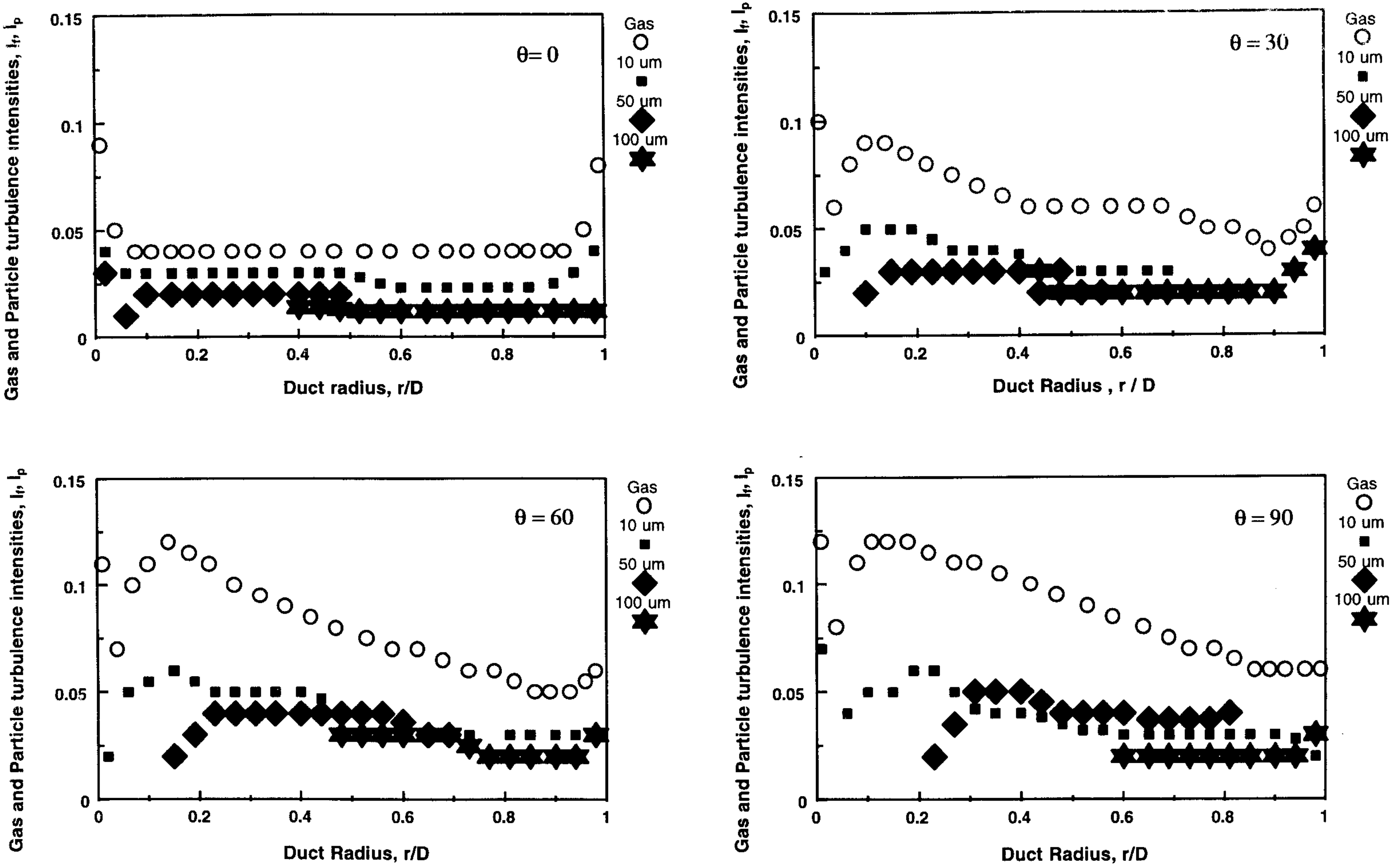

Figure 9. Gas and particle turbulence intensity distributions in the curved duct.

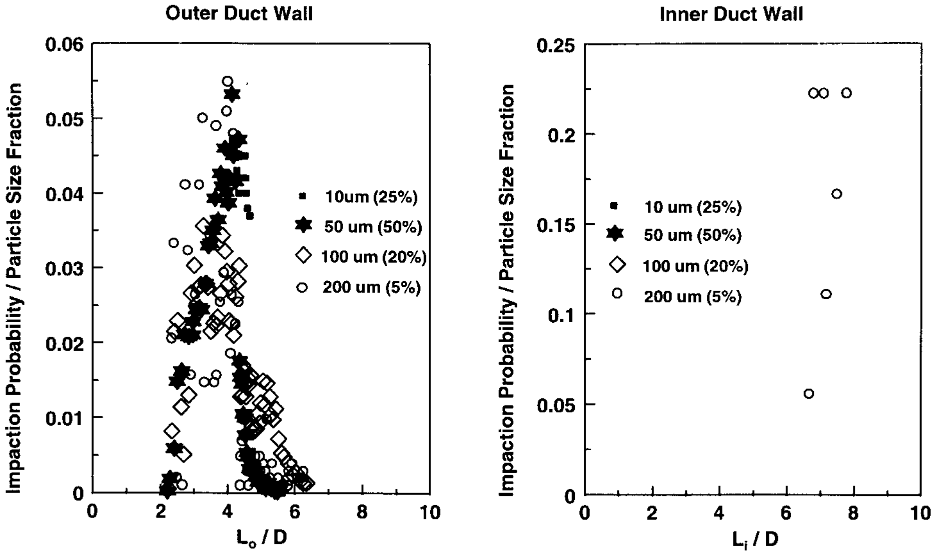

Figure 10. Impaction probabilities of all the particle sizes with the walls of the curved duct.

As the flow progresses through the curved duct section, high gas turbulence intensities are obtained at the inner wall, which decay towards the duct centreline. For the particulate phase, particles of all sizes also have similar distributions, except that their magnitudes are much lower. Towards the bend outlet ($\theta = 90°$), the larger particle sizes are much more concentrated at the duct centreline and the outer wall due to the centrifuging effect, and here they still retain a turbulence intensity distribution profile similar to the gas phase.

### *3.6. Particle impaction*

In the present study, the erosion process is not modelled, but the flow of the particles and their impaction characteristics have been computed. The distribution of the particle impactions with the duct walls are indicated by Figure 10, where particle impaction has been defined as a impaction probability parameter of the particle size fraction At the outer wall of the curved section, it is evident that the heavier particles strike the outer wall first with the majority of the smaller sizes striking further downstream. For the larger particle sizes, the impactions are dominated by their inertia, and after impaction they rebound from the wall and become re-entrained into the main flow. Some of the smaller 10 μm particles also strike the outer wall, but further downstream from the bend outlet. This impaction is largely due to the eddy impaction process, where particles can penetrate the boundary layer only if they possess a 'stopping distance' that is greater than the boundary layer thickness. On this duct outer wall, the main impaction regime for the all the particle sizes are predicted to be within a outer duct length of two to six times the duct diameter.

At the inner wall, particle impaction occurs near the vertical outlet section. This occurs only with the 200 μm particles that have rebounded from the outer wall within the curved section of the duct (see Figure 6). The trend in the probability of particle impactions at the outer wall in Figure 10 are in qualitative agreement with the erosion rates observed by Mason and Smith [9], who show that erosion rates initially increase with $\theta$ and reaches a maximum at about 20–30°, whereafter it reduces sharply. From predicted particle velocities, mass fluxes, angles of impact and wall mechanical properties, Pourahmadi and Humphrey [8] also showed that with Finnie's [37] wear model, qualitatively similar trends were obtained in the relative erosion rates as observed by Mason and Smith [9].

## 4. CONCLUSIONS

The flow of a gas–solid mixture has been numerically predicted in two geometrical configurations utilising the Eulerian–Lagrangian methodology. By assuming that the particulate phase is dilute and that the particle to gas density ratios are much greater than unity, the governing momentum equations for the particulate phase have been solved with appropriately prescribed boundary conditions. The influence of fluid turbulence on particle dispersion was represented by a statistical model that accounts for both the turbulent eddy lifetime and the particle transit time scale.

Initially, a dilute gas–solids flow in a vertical duct was simulated. Comparisons of the predicted gas and particulate phase mean velocities and turbulent intensities with experimental LDV data of Tusiji *et al.* [4] show a reasonably good agreement. The flow of an isothermal dilute gas–solid mixture consisting of several particle sizes was subsequently simulated in a strongly curved duct. For the smaller particles, the computed mean velocities indicate that their interslip velocities are small and their particle trajectories generally coincide with the fluid streamlines. The dispersion of the smaller particles is also quite significant within the duct. The larger particles, however, have much higher interslip velocities and strongly deviate from the fluid streamlines, which is as a consequence of their inertia. As expected, their dispersion is small in comparison with the smaller particle sizes, due to their insensitivity to the turbulent eddies. The frequency of the particles striking the duct walls particularly the outer wall of the curved duct section, increases as the particle sizes increase. At the outer wall, the main impaction zone for the all the particle sizes is predicted to be within an outer duct length of two to six times the duct diameter.

## APPENDIX A. NOMENCLATURE

| | |
|---|---|
| $a$ | coefficients in Equation (11) |
| $A_\mathrm{p}$ | projected area of particle ($\mathrm{m}^2$) |
| $C_\mathrm{D}$ | particle drag coefficient |
| $C_\mu$ | constant |
| $d_\mathrm{p}$ | diameter of particle (m) |
| $D$ | duct width (m) |
| $g_i$ | gravity vector ($\mathrm{m\,s}^{-2}$) |
| $I_\mathrm{f}^p$, $I_\mathrm{p}^p$ | gas and particle turbulence intensities, $\overline{v_\mathrm{f}^2}/U_\mathrm{c}$, $\overline{v_\mathrm{p}^2}/U_\mathrm{c}$ |
| $I_\mathrm{f}$, $I_\mathrm{p}$ | gas and particle turbulence intensities, $\overline{v_\mathrm{f}^2}/U_\mathrm{o}$, $\overline{v_\mathrm{p}^2}/U_\mathrm{o}$ |
| $J$ | Jacobian of co-ordinate transformation |
| $k$ | kinetic energy of turbulence ($\mathrm{m}^2\,\mathrm{s}^{-2}$) |
| $l_\mathrm{e}$ | eddy length scale (m) |
| $L_\mathrm{i}$, $L_\mathrm{o}$ | inner and outer longitudinal length of duct (m) |

| | |
|---|---|
| $m_{\mathrm{p}}$ | mass of particle (kg) |
| $P$ | pressure ($\mathrm{N\,m^{-2}}$) |
| $Re$ | particle Reynolds number |
| $r$ | distance between inner and outer walls of pipe (m) |
| $S$ | source term in Equation (11) |
| $t$ | time (s) |
| $t_{\mathrm{int}}$, $t_{\mathrm{e}}$, $t_{\mathrm{r}}$ | interaction, eddy and transit times (s) |
| $u$ | gas velocity vector ($\mathrm{m\,s^{-1}}$) |
| $U$ | mean axial gas or particle velocity in pipe ($\mathrm{m\,s^{-1}}$) |
| $U_{\mathrm{c}}$ | centreline gas velocity in pipe ($\mathrm{m\,s^{-1}}$) |
| $U_{\mathrm{abs}}$ | absolute gas velocity ($\mathrm{m\,s^{-1}}$) |
| $U_{\mathrm{o}}$ | mean gas velocity at duct inlet ($\mathrm{m\,s^{-1}}$) |
| $U_{\mathrm{p}}$, $V_{\mathrm{p}}$ | mean particle velocities in the $x$- and $y$-directions ($\mathrm{m\,s^{-1}}$) |
| $V_{\mathrm{p}i}$ | instantaneous particle velocity vector ($\mathrm{m\,s^{-1}}$) |
| $V_{\mathrm{f}i}$ | instantaneous gas velocity vector ($\mathrm{m\,s^{-1}}$) |
| $v_{\mathrm{f}i}$, $v_{\mathrm{p}i}$ | fluctuating gas and particle velocity vector ($\mathrm{m\,s^{-1}}$) |
| $\bar{v}_{\mathrm{f}}$, $\bar{v}_{\mathrm{p}}$ | absolute gas and particle fluctuating velocities ($\mathrm{m\,s^{-1}}$) |
| $\bar{V}_{\mathrm{f}i}$ | mean gas velocity vector ($\mathrm{m\,s^{-1}}$) |
| $x, y$ | Cartesian co-ordinates (m) |
| $x_{\mathrm{p}i}$ | co-ordinate vector of the particle (m) |
| $y^{+}$ | dimensionless normal distance from wall |

*Greek letters*

| | |
|---|---|
| $\alpha$ | prescribed time step factor |
| $\beta$ | co-factors of co-ordinate transformation |
| $\delta$ | Kronecker's delta |
| $\varepsilon$ | dissipation of fluid turbulent kinetic energy ($\mathrm{m^2\,s^{-3}}$) |
| $\phi$ | shape function for quadrilateral element |
| $\mu$ | fluid dynamic viscosity ($\mathrm{kg\,m^{-1}\,s^{-1}}$) |
| $\mu_{\mathrm{eff}}$ | effective viscosity ($\mathrm{kg\,m^{-1}\,s^{-1}}$) |
| $\mu_{\mathrm{T}}$ | turbulent viscosity ($\mathrm{kg\,m^{-1}\,s^{-1}}$) |
| $\theta$ | inclination of wall surface (°) |
| $\rho$ | density of the fluid ($\mathrm{kg\,m^{-3}}$) |
| $\rho_{\mathrm{p}}$ | density of the particle ($\mathrm{kg\,m^{-3}}$) |
| $\sigma_{\varepsilon}$ | Prandtl/Schmidt number for $\varepsilon$ |
| $\sigma_{k}$ | Prandtl/Schmidt number for k |
| $\sigma_{i}$ | normally distributed random number |
| $\tau$ | particle response time (s) |
| $\xi, \eta$ | local non-orthogonal co-ordinates |
| $\Delta x$, $\Delta y$ | length and width of a computational cell (m) |

*Subscripts*

| | |
|---|---|
| $i, j$ | co-ordinate directions or tensor indices |
| $l, m, n$ | tensor indices |

## REFERENCES

1. J.A.C. Humphrey, J.H. Whitelaw and Y. Lee, 'Turbulent flow in a square duct with strong curvature', *J. Fluid Mech.*, **103**, 443–463 (1981).
2. J.A.C. Humphrey, A.M.K. Taylor and J.H. Whitelaw, 'Laminar flow in a square duct of strong curvature', *J. Fluid Mech.*, **83**, 509–527 (1977).
3. R. Platfoot and C.A.J. Fletcher, 'Gas flows within turning section', *Int. J. Numer. Methods Heat Fluid Flow*, **1**, 19–29 (1991).
4. Y. Tsuji, Y. Morikawa and H. Shimoni, 'LDV measurements of an air–solid two-phase flow in a vertical pipe', *J. Fluid Mech.*, **139**, 417–434 (1984).
5. S.L. Lee and F. Durst, 'On the motion of particles in turbulent duct flows', *Int. J. Multiphase Flows*, **8**, 125 (1982).
6. M. Maeda, K. Hishida and T. Furutani, 'Optical measurements of local gas and particle velocity in an upward flowing dilute gas–solids suspension', *Proc. Polyphase Flow and Transport Technology*, San Francisco, CA, 1980, pp. 211–215.
7. Y. Tsuji and Y. Morikawa, 'LDV measurements of an air–solid two-phase flow in a horizontal pipe', *J. Fluid. Mech.*, **120**, 385 (1982).
8. F. Pourahmadi and J.A.C. Humphrey, 'Modelling solid–fluid turbulent flows with application to predicting erosive wear', *PCH Phys. Chem. Hydrodyn.*, **4**, 191–219 (1983).
9. J.S. Mason and B.V. Smith, 'The erosion of bends by pneumatically conveyed suspensions of abrasive particles', *Powder Technol.*, **6**, 323–335 (1972).
10. J.A.C. Humphrey, 'Fundamentals of fluid motion in erosion by solid particle impact', *Int. J. Heat Fluid Flow*, **2**, 120–195 (1990).
11. M.J. Schuh, C.A. Schuler and J.A.C. Humphrey, 'Numerical calculation of two-phase flow and erosion in particle laden flow past tubes', *AIChE J.*, **35**, 466–480 (1989).
12. B. Beacher, W. Tabakoff and A. Hamed, 'Improved particle trajectories calculations through turbomachinery affected by coal ash particles', *ASME J. Eng. Power*, **104**, 64–68 (1982).
13. J.Y. Tu and C.A.J. Fletcher, 'Numerical computation of turbulent gas–solid particle flow in a 90° bend', *AIChE J.*, **41**, 2187–2197 (1995).
14. Y. Kliafas and M. Holt, 'LDV measurements of a turbulent air–solid two-phase flow in a 90° bend', *Exp. Fluids*, **5**, 73–83 (1987).
15. D. Migdal and A.D. Agosta, 'A source flow model for continuum gas–particle flow', *Trans. ASME J. Appl. Mech.*, 860–865 (1967).
16. C.T. Crowe, M.P. Sharma and D.E. Stock, 'The particle-source-in-cell model for gas-droplet flows', *Trans. ASME J. Fluids Eng.*, 325–332 (1977).
17. Y. Pan and S. Banerjee, 'Numerical investigation of the effects of large particles on wall turbulence', *Phys. Fluids*, **9**, 3786–3807 (1997).
18. S. Elghobashi and G.C. Truesdell, 'On the two-way interaction between homogeneous turbulence and dispersed solid particles. 1: Turbulence modification', *Phys. Fluid A*, **5**, 1790–1801 (1993).
19. M. Peric, R. Kessler and G. Scheurer, 'Comparisons of finite volume numerical methods with staggered and collocated grids', *Comput. Fluids*, **16**, 389–403 (1988).
20. W. Rodi, S. Mujumdar and B. Schonung, 'Finite volume methods for two-dimensional incompressible flows with complex boundaries', *Comput. Methods Appl. Mech. Eng.*, **75**, 369–392 (1989).
21. S. Majumdar, W. Rodi, and J. Zhu, 'Three-dimensional finite volume method for incompressible flows with complex boundaries', *ASME J. Fluids Eng.*, **114**, 496–503 (1992).
22. W.P. Jones and B.E. Launder, 'The prediction of laminarisation with a two-equation model of turbulence', *Int. J. Heat Mass Transf.*, **5**, 301–312 (1972).
23. B.E. Launder and D.B. Spalding, 'The numerical computations of turbulent flows', *Comput. Methods Appl. Mech. Eng.*, **3**, 200–212 (1974).
24. S.V. Patankar, *Numerical Heat Transfer and Fluid Flow*, McGraw-Hill, New York, 1980.
25. A.D. Gosman, W.M. Pun, A.K. Runchal, D.B. Spalding and M. Wolfstein, *Heat and Mass Transfer in Recirculating Flows*, Academic Press, London, 1969.
26. C.M. Rhie and W.L. Chow, 'A numerical study of the turbulent flow past an isolated airfoil with trailing edge separation', *J. AIAA*, **AIAA-82-0998**, 1525–1532 (1982).
27. S.V. Patankar and D.B. Spalding, 'A calculation procedure for heat, mass and momentum transfer in three-dimensional parabolic flows', *Int. J. Heat Mass Transf.*, **15**, 1787–1797 (1972).
28. M. Peric, 'Analysis of pressure–velocity coupling on non-orthogonal grids', *Numer. Heat Transf. B*, **17**, 63–82 (1990).
29. H.L. Stone, 'Iterative solution of implicit approximations of multi-dimensional partial differential equations', *SIAM J. Numer. Anal.*, **5**, 530–542 (1968).
30. R. Clift, J.R. Grace and M.E. Weber, *Bubbles, Drops and Particles*, Academic Press, New York, 1973.
31. C.J. Lawn, *Principles of Combustion Engineering for Boilers*, Academic Press, New York, 1987.
32. J.K. Duckowicz, 'A particle–fluid numerical model for liquid sprays', *J. Comput. Phys.*, **35**, 229–253 (1980).
33. A.D. Gosman and E. Ioannides, 'Aspects of computer simulation of liquid fueled combustors', *AIAA Paper 81-0323*, 19th Aerospace Sciences Meeting, 1981.

34. S.K. Friedlander and H.F. Johnstone, 'Deposition of suspended particles from turbulent gas streams', *Ind. Eng. Chem.*, **49**, 1151–1156 (1957).
35. H. Brauer, 'Report on investigations on particle movement in straight horizontal tubes, particle–wall collision and erosion of tubes and bends', *J. Powder Bulk Solids Technol.*, **4**, 3–12 (1980).
36. J.E. Akin, *Applications and Implementation of Finite Element Methods*, Academic Press, New York, 1982.
37. I. Finnie, 'Some observations on the erosion of ductile metals', *Wear*, **19**, 81–89 (1972).